New Journal of Physics
The open access journal at the forefront of physics

Deutsche Physikalische Gesellschaft DPG IOP Institute of Physics

PAPER • OPEN ACCESS

Distortion of the local density of states in a plasmonic cavity by a quantum emitter

To cite this article: Alvaro Cuartero-González *et al* 2021 *New J. Phys.* **23** 073011

New Journal of Physics
The open access journal at the forefront of physics

Deutsche Physikalische Gesellschaft DPG
IOP Institute of Physics

Published in partnership with: Deutsche Physikalische Gesellschaft and the Institute of Physics

OPEN ACCESS

RECEIVED
11 March 2021

REVISED
28 April 2021

ACCEPTED FOR PUBLICATION
14 May 2021

PUBLISHED
19 July 2021

PAPER

Distortion of the local density of states in a plasmonic cavity by a quantum emitter

Alvaro Cuartero-González[1,*], Alejandro Manjavacas[2,3] and Antonio I Fernández-Domínguez[1]

[1] Departamento de Física Teórica de la Materia Condensada and Condensed Matter Physics Center (IFIMAC), Universidad Autónoma de Madrid, 28049 Madrid, Spain
[2] Instituto de Óptica (IO-CSIC), Consejo Superior de Investigaciones Científicas, 28006 Madrid, Spain
[3] Department of Physics and Astronomy, University of New Mexico, Albuquerque, New Mexico 87106, United States of America
[*] Author to whom any correspondence should be addressed.

E-mail: alvaro.cuartero@uam.es

Keywords: plasmonics, density of states, quantum emitters

Abstract

We investigate how the local density of states in a plasmonic cavity changes due to the presence of a distorting quantum emitter. To this end, we use first-order scattering theory involving electromagnetic Green's function tensors for the bare cavity connecting the positions of the emitter that distorts the density of states and the one that probes it. The confined, quasistatic character of the plasmonic modes enables us to write the density of states as a Lorentzian sum. This way, we identify three different mechanisms behind the asymmetric spectral features emerging due to the emitter distortion: the modification of the plasmonic coupling to the probing emitter, the emergence of modal-like quadratic contributions and the absorption by the distorting emitter. We apply our theory to the study of two different systems (nanoparticle-on-mirror and asymmetric bow-tie-like geometries) to show the generality of our approach, whose validity is tested against numerical simulations. Finally, we provide an interpretation of our results in terms of a Hamiltonian model describing the distorted cavity.

1. Introduction

During the past decade, plasmonic cavities emerged as one of the key platforms to both explore and exploit light–matter interactions at the nanoscale, giving rise to a plethora of plasmonic-based research and applications in areas such as optomechanics [1], biosensing [2, 3] or spectroscopy [4–6]. Those rely on the remarkable strength of plasmon–emitter interactions originating from the subwavelength field confinement that takes place in metallic nanostructures. Despite the relatively large losses associated to metals, this light shrinking allows to probe the coupling between electromagnetic (EM) fields and quantum emitters (QEs), even to the limits where those reveal their inner structure [7–13]. On the other hand, the emission properties of QEs are not inherent to them. It is well known that plasmonic modes sustained by nanocavities modify their emission properties through Purcell effect, which implies that the characteristics of the light radiated by QEs depend on the photonic local density of states (LDOS) in their surroundings [14, 15]. Recent theoretical reports have also revealed the key role played by the LDOS in molecule interactions in resonant cavities [16, 17].

The spatial and spectral properties of the LDOSs associated to nanocavities (where both metal and dielectric media coexist) result from the interplay between the wavelength of the EM fields, λ, and the length scale of the system, L, characterized by the ratio $\xi = L/\lambda$. Plasmonic nanocavities typically operate in the quasistatic limit ($\xi \ll 1$), in which metal absorption yields an LDOS composed of a number of symmetric Lorentzian-shaped peaks [8, 18, 19], which admits quantization in terms of non-interacting bosonic modes [20–23]. On the other hand, in photonic crystals and larger cavities ($\xi \gtrsim 1$), fully electrodynamic interference and retardation effects give rise to asymmetric and Fano-like lineshapes, as

those reported in references [24, 25]. It has been recently shown that non-Lorentzian-like spectral features can be described using general Hamiltonians involving interacting photonic modes [26, 27]. In the context of PT-symmetric exceptional points, theoretical reports have revealed that quadratic Lorentzian contributions [28] emerge in the LDOS of resonators combining optical gain and loss [29].

From the experimental perspective, the development of different nanofabrication techniques [30–33] is progressively overcoming the difficulties inherent to the control of both the exact number of QEs as far as their exact position and orientation inside a nanocavity. This way, innovative structures have led to novel scenarios for light–matter interactions. Recent experiments reached the strong coupling regime [34] in the limit of very few or even single QEs at room temperature [35, 36] within the field of plasmonic cavities. Moreover, it has been shown that hybrid structures [37, 38] and photonic crystals [25] provide new means for the spectral design of LDOS. The efficient control of light emission procured by those systems open new roads for quantum information technologies [39–41] not only at the few emitter level, but also for mesoscopic QE ensembles [42]. This fact is especially relevant in the context of the emergent field of quantum optical metamaterials [43, 44].

In this article, we present a theoretical study of how the presence of a QE can distort the LDOS in a plasmonic cavity. Firstly, due to its experimental relevance, we focus our attention on the nanoparticle-on-mirror (NPoM) geometry. We will exploit that the optical response of its two-dimensional counterpart can be described analytically by means of transformation optics in the quasistatic limit ($\xi \ll 1$) [23, 45, 46]. We quantify the distortion due to the QE through the so-called generalized Purcell factor [24, 28] (defined as the LDOS normalized to its free-space value) and the spectral density $J(\omega)$. Those quantities are calculated through first-order scattering theory applied to the EM Green's function of the bare cavity. Exploiting the quasistatic character of the NPoM plasmonic modes we write it as a sum of complex Lorentzians. While $J(\omega)$ of the bare cavity presents only symmetric Lorentzian peaks, our theory reveals that non-Lorentzian terms arise due to the distorting emitter. We unveil three different mechanisms behind these features, yielding asymmetric profiles even in this deeply subwavelength system. Finally, to prove the generality of the physical phenomena found in the NPoM case, we consider an asymmetric bow-tie-like three-dimensional architecture, whose analytical treatment is not possible. Applying the same scattering formalism, we obtain $J(\omega)$ of this hybrid QE-cavity system. We check our results against full-numerical EM simulations in which the distorting emitter is modelled through an effective permittivity defined to reproduce the free-space polarizability of an absorbing two level system.

2. Theoretical frame

2.1. Scattering formalism for the Dyadic Green's function

The general form of the system under study is presented in figure 1(a): two QEs interacting with a nanocavity that sustains plasmonic resonances. The first QE probes the LDOS of the hybrid system composed by the nanostructure and the second QE. Our focus will be in analysing how this emitter distorts the spectral density of the bare cavity. The metallic resonator, embedded in a surrounding medium ($\epsilon_r = 1$), is described through a Drude-fitting to Ag permittivity of the form $\epsilon(\omega) = \epsilon_\infty - \omega_p^2/(\omega(\omega + i\gamma_m))$ with parameters $\epsilon_\infty = 9.7$, $\omega_p = 8.91$ eV and $\gamma_m = 0.06$ eV. In general, we use the convention $\hbar = 1$ and any parameter related to frequency will have energy dimensions. The probing and distorting QEs are characterized by their dipole momenta ($\boldsymbol{\mu} = \mu\hat{\mathbf{n}}_\mu, \boldsymbol{\mu}_E = \mu_E\hat{\mathbf{n}}_E$), their respective transition frequencies (ω, ω_E) and their positions ($\mathbf{r}, \mathbf{r}_E$). This path opens the possibility of studying the problem in terms of Green's function tensor $\mathbf{G}(\mathbf{r}, \mathbf{r}, \omega)$. We assume that the interaction between the cavity plasmons and the distorting emitter is weak, which allows us to express the system EM Green's function tensor through the first-order correction in scattering theory. Moreover, in the single-excitation subspace, the distorting QE, $\boldsymbol{\mu}_E$, is modelled through an atom-like polarizability in the form $\alpha_E(\omega) = \frac{\mu_E^2}{\hbar}\mathcal{L}_E(\omega)$, where $\mathcal{L}_E(\omega) = \frac{1}{(\omega_E - i\gamma_E/2) - \omega}$ is the complex Lorentzian function defined by ω_E and γ_E, the absorption linewidth [47]. Thus, we are able to write the Green's function tensor for the hybrid cavity-QE system, $\mathbf{G}_{II}(\mathbf{r}, \mathbf{r}, \omega)$, in terms of its counterpart for the bare cavity, $\mathbf{G}_I(\mathbf{r}, \mathbf{r}, \omega)$ [48, 49],

$$\mathbf{G}_{II}(\mathbf{r}, \mathbf{r}, \omega) = \mathbf{G}_I(\mathbf{r}, \mathbf{r}, \omega) + \Psi_0\mathbf{G}_I(\mathbf{r}, \mathbf{r}_E, \omega)\tilde{\boldsymbol{\alpha}}_E(\omega)\mathbf{G}_I(\mathbf{r}_E, \mathbf{r}, \omega), \tag{1}$$

where Ψ_0 is a frequency dependent factor which depends on the problem dimensionality. It takes the values $\Psi_0 = \frac{\omega^2}{\epsilon_0 c^2}$ for three-dimensional (3D) calculations or $\Psi_0 = \frac{4\omega^3}{3\pi\epsilon_0 c^3}$ if we consider two-dimensional (2D) systems. The polarizability tensor reads $\tilde{\boldsymbol{\alpha}}_E(\omega) = \tilde{\alpha}_E(\omega)\mathbf{T}(\hat{\mathbf{n}}_E)$ where $\tilde{\alpha}_E(\omega) = \alpha_E(\omega)/\left(1 - i\beta_I(\mathbf{r}_E, \mathbf{r}_E, \omega)\alpha_E(\omega)\right)$ and the tensor $[\mathbf{T}(\hat{\mathbf{n}}_E)]_{ij} = [\hat{\mathbf{n}}_E]_i\delta_{ij}$ accounts for the orientation of the distorting QE (δ_{ij} is Kronecker delta). Note that $\beta_I(\mathbf{r}_E, \mathbf{r}_E, \omega) = \Psi_0\,\mathrm{Im}\{\hat{\mathbf{n}}_E\mathbf{G}_I(\mathbf{r}_E, \mathbf{r}_E, \omega)\hat{\mathbf{n}}_E\}$ plays the role of the so-called depolarization tensor in scattering theory [50, 51], introducing a radiative-reaction

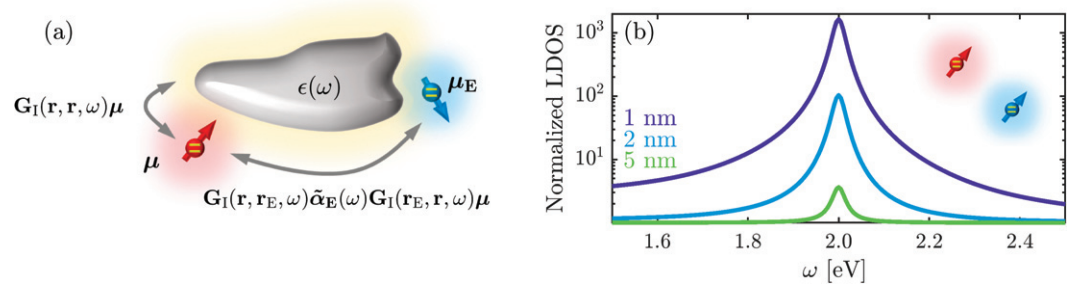

Figure 1. Motivation. (a) Sketch of the system under study. A QE, $\boldsymbol{\mu}$, probes the LDOS of a plasmonic cavity, with metal permittivity $\epsilon(\omega)$, modified by the presence of a second emitter, $\boldsymbol{\mu}_{\mathbf{E}}$. Grey arrows sketch the two terms in the first-order scattering theory description of the total Green's function. (b) Normalized LDOS experienced by an emitter in free space when a second, parallel one, is placed in its surroundings. Colour code (indicated in the legend) corresponds to different separations between emitters ($\mathbf{d} = (\mathbf{r}_{\mathrm{E}} - \mathbf{r}) \perp \boldsymbol{\mu}$).

correction to the free-space QE polarizability [52]. It is expressed in terms of the bare cavity Green's function, and therefore does not only account for far-field radiation losses but mainly for near-field plasmonic absorption. As discussed above, the Purcell factor corresponds to the normalized LDOS. This is defined as $P_i^{\mathrm{f}}(\omega) = \mathrm{Im}\{\hat{\mathbf{n}}_\mu \mathbf{G}_i(\mathbf{r},\mathbf{r},\omega)\hat{\mathbf{n}}_\mu\}/\mathrm{Im}\{\hat{\mathbf{n}}_\mu \mathbf{G}_0(\mathbf{r},\mathbf{r},\omega)\hat{\mathbf{n}}_\mu\}$. $\mathbf{G}_0(\mathbf{r},\mathbf{r}',\omega) = [\mathbf{I} + \frac{c^2}{\omega^2}\nabla\nabla]G_0(\mathbf{r},\mathbf{r}',\omega)$ is the Green's function tensor in free space, where $G_0(\mathbf{r},\mathbf{r}',\omega)$ is the scalar Helmholtz Green's function. Index $i = \mathrm{I}, \mathrm{II}$ refers to the bare and QE-distorted cavity, respectively. Figure 1(b) shows the modification of the free-space LDOS by a single QE, i.e. $\mathbf{G}_{\mathrm{I}}(\mathbf{r},\mathbf{r}_{\mathrm{E}},\omega) = \mathbf{G}_0(\mathbf{r},\mathbf{r}_{\mathrm{E}},\omega)$ in equation (1). A Purcell factor peak emerges in the spectrum, that inherits its Lorentzian-like shape from the QE absorption lineshape. Throughout this work, the QE parameters ($\mu_{\mathrm{E}} = 0.4$ e nm, $\gamma_{\mathrm{E}} = 0.03$ eV) are set in agreement with recent experimental characterization of dye molecules [53]. The dipole moments of both QEs are parallel to each other ($\hat{\mathbf{n}}_\mu \| \hat{\mathbf{n}}_{\mathrm{E}}$) and $\mathbf{d} = (\mathbf{r}_{\mathrm{E}} - \mathbf{r}) \perp \hat{\mathbf{n}}_\mu$. The height of the LDOS maximum is set by the dipole moment strength of the distorting QE and $|\mathbf{d}|$, the distance between the emitters, for which we chose three different values. We can observe Purcell enhancements as large as 10^3 for QE–QE distances as small as 1 nm.

2.2. Full electrodynamic solutions

In order to check the validity of our scattering approach, we perform finite-element simulations using COMSOL Multiphysics. In our numerical calculations, the probing QE, $\boldsymbol{\mu}$, is treated as a dipolar EM source in the presence of the bare metal cavity. Then, we add an spherical particle with radius a as the object that effectively simulates the absorbing character of the distorting QE, $\boldsymbol{\mu}_{\mathrm{E}}$. Its effective permittivity is chosen to match the atom-like polarizability. Using the quasistatic scattering of a dielectric sphere under plane-wave illumination, we can write $\alpha_{\mathrm{E}}(\omega) = 4\pi\epsilon_0 a^3 \frac{\epsilon_{\mathrm{eff}}(\omega)-1}{\epsilon_{\mathrm{eff}}(\omega)+2}$, or $\epsilon_{\mathrm{eff}}(\omega) = \frac{1+2\eta_{3\mathrm{D}}(\omega)}{1-\eta_{3\mathrm{D}}(\omega)}$, where $\eta_{3\mathrm{D}}(\omega) = \frac{\alpha_{\mathrm{E}}(\omega)}{4\pi\epsilon_0 a^3}$. The value of the free parameter a is set by means of free-space calculations similar to those in figure 1(b). The radius of the distorting QE is made small enough to reach convergence in the Purcell factor spectrum. Note that the effective permittivity used for simulations does not require the introduction of radiative reaction corrections, since those emerge naturally in the numerical solution. Our model is similar to others, applied for phenomena such as plasmon–QE strong coupling [54], plasmon-assisted FRET [55], near-field exciton harvesting [56] and energy transfer in nanocrystals [57]. We employ this modelling scheme also to test our 2D analytical calculations for the NPoM cavity. In this case, the relationship between the polarizability and the permittivity of the distorting QE is $\frac{4\omega}{3\pi c}\alpha_{\mathrm{E}}(\omega) = 2\pi\epsilon_0 a^2 \frac{\epsilon_{\mathrm{eff}}(\omega)-1}{\epsilon_{\mathrm{eff}}(\omega)+1}$, where $\frac{4\omega}{3\pi c}$ is the value of the ratio between 2D and 3D Ψ_0 factors, needed for dimensionality correctness. In this case, the effective permittivity has the form $\epsilon_{\mathrm{eff}}(\omega) = \frac{1+\eta_{2\mathrm{D}}(\omega)}{1-\eta_{2\mathrm{D}}(\omega)}$ with $\eta_{2\mathrm{D}}(\omega) = \frac{4\omega}{3\pi c}\frac{\alpha_{\mathrm{E}}(\omega)}{2\pi\epsilon_0 a^2}$.

3. Emitter distortion of Purcell factor: NPoM case

We use the formalism above to study the Purcell factor experienced by the emitter $\boldsymbol{\mu}$ in a NPoM cavity hosting the emitter $\boldsymbol{\mu}_{\mathrm{E}}$. The system is characterised by the following geometrical parameters: D, diameter of the particle, δ, gap size between the particle and the mirror plane, and the positions of the probing and distorting QEs, $\mathbf{r}$ and $\mathbf{r}_{\mathrm{E}}$, respectively.

Figure 2(a) shows the variety of effects that the presence of the distorting QE in the vicinity of the NPoM cavity can produce in the near-field emission spectrum (mainly into non-radiative channels) of the probing one. The inset presents a sketch of the cavity and the emitters. Black to grey dotted lines corresponds to normalized LDOS spectra for an emitter in different cavities ($D = 35$ nm and increasing δ,

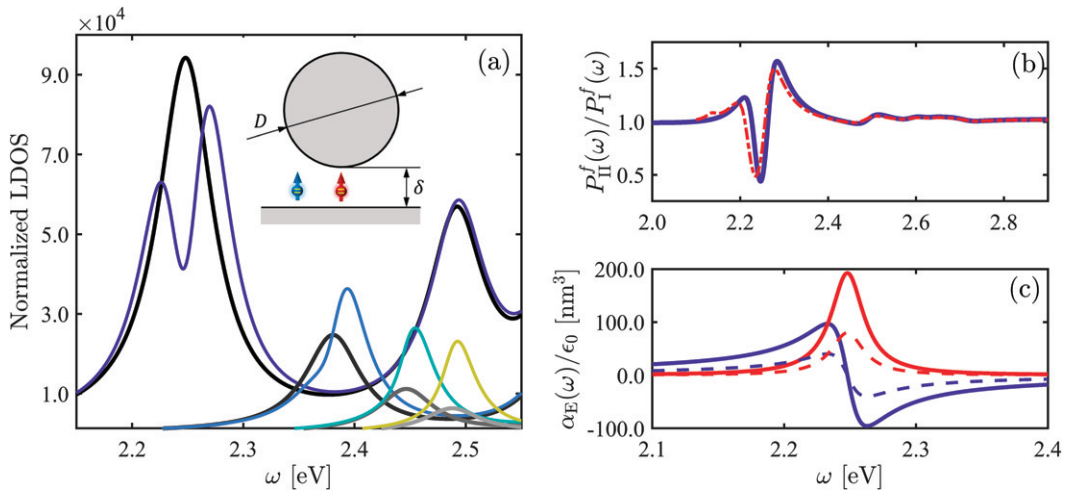

Figure 2. LDOS distortion in NPoM. (a) Normalized LDOS spectra for NPoM cavities with $D = 35$ nm and different gap sizes ($\delta \in [1, 4]$ nm from dark blue to yellow) for a vertical QE at the gap centre. Black to grey dotted lines represent $P^f_I(\omega)$. Blue to yellow lines show $P^f_{II}(\omega)$, corresponding to the distorted spectra due to a QE, displaced 0.5 nm horizontally from the probing one. (b) $P^f_{II}(\omega)/P^f_I(\omega)$ for $D = 35$ nm and $\delta = 1$ nm. The blue solid line corresponds to full electrodynamic calculations and the red dotted one is the scattering theory calculation in the quasistatic limit. (c) Red and blue solid lines plot the real and imaginary parts of the polarizability $\alpha_E(\omega)$ for the case $\omega_E = 2.25$ eV. Dashed lines show the same components of $\tilde{\alpha}_E(\omega)$, corrected due to the depolarization field induced in the cavity.

from 1 to 4 nm in 1 nm steps), placed at the centre of the gap and oriented along the vertical direction. The LDOS of the bare cavity is composed by a set of plasmonic modes characterized by their azymuthal order n and their frequency ω_n, analysed in detail in reference [23]. The lowest energy peak corresponds to the dipolar plasmon (ω_1) and its contribution increases and redshifts as the gap size shrinks. Dark blue to yellow lines represent the Purcell spectra for the same cavities but considering the hybrid scenario, with the presence of $\boldsymbol{\mu}_E$ at a horizontal distance $|\mathbf{d}| = 0.5$ nm. The distorting QE is vertically oriented and characterized by the same parameters as in figure 1(b) with $\omega_E = \omega_1$, i.e. it is always at resonance with the lowest plasmon mode. For small gaps, comparable to those realized experimentally to achieve plasmon–exciton strong coupling, the presence of $\boldsymbol{\mu}_E$ causes a clear dip in the spectra. As the gap size increases, the dip disappears and the $\boldsymbol{\mu}_E$ causes both an enhancement and blueshifting with respect to the bare cavity LDOS maximum at ω_1. This result demonstrates that the presence of more than one emitter interacting with gap plasmons can enrich the light–matter coupling phenomenology, effectively increasing or decreasing the LDOS depending on the cavity configuration. As explained in section 2.2, we performed numerical calculations by using COMSOL Multiphysics in order to check these results. Figure 2(b) shows the distorted LDOS normalized to the bare cavity one, equivalent to the ratio $P^f_{II}(\omega)/P^f_I(\omega)$ between the Purcell factors for the hybrid cavity-QE and bare cavity systems for the case $\delta = 1$ nm. Blue solid line corresponds to the numerical calculation and red dotted one to our scattering theory approach. They are in almost perfect agreement. Figure 2(c) plots both real and imaginary parts of $\alpha_E(\omega)$ in solid blue and red, respectively. Dashed lines display $\tilde{\alpha}_E(\omega)$ for $\delta = 1$ nm when considering the correction $1 + \beta_I(\mathbf{r}_E, \mathbf{r}_E, \omega_E)\mathrm{Im}\{\alpha_E(\omega_E)\}$. In this configuration, the radiative correction is the strongest, but the polarizability keeps its Lorentzian functional form (see section 4). It is clear that the action of the depolarization field is relevant in the nanometric gaps in figure 2(b).

The analytical character of the our approach permits us to explore the full set of parameters that define the LDOS. Inspired by the experimental setups in which plasmon–emitter strong coupling has been reported [35, 36], we focus on cavity configurations where the probing QE is placed at the gap centre. In figure 3, we explore NPoMs ($D = 35$ nm and $\delta = 1.5$ nm) in which the distorting QE is around this symmetric position. It presents an exhaustive scan of the effects of the distorting emitter on the Purcell factor. As in figure 2, we centre our attention on the case $\omega_E = \omega_1$ and both $\boldsymbol{\mu}$ and $\boldsymbol{\mu}_E$ oriented along the vertical direction. The solid blue-to-yellow lines in figure 3(a) represent the different Purcell spectra $P^f_{II}(\omega)$ as $\boldsymbol{\mu}_E$ is displaced horizontally (see the relative positions in the inset) while black line corresponds to $P^f_I(\omega)$. The dip produced by the emitter changes its character (from asymmetric to symmetric) and finally disappears as the QE–QE separation increases. The interplay between the free-space (dominant for the smallest separations) and plasmonic contribution to $\mathbf{G}_I(\mathbf{r}_E, \mathbf{r}, \omega)$ provides the difference in the spectral features. When both emitters are far from each other (not shown here), $\boldsymbol{\mu}_E$ becomes decoupled from the cavity fields and $\mathbf{G}_I(\mathbf{r}_E, \mathbf{r}, \omega)$ is negligible.

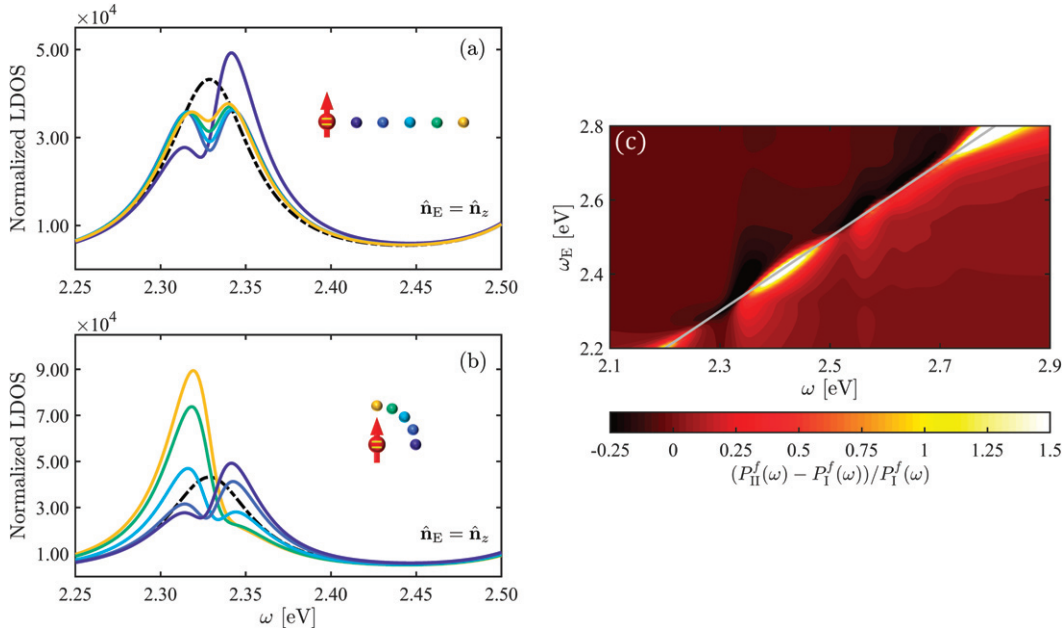

Figure 3. LDOS dependence on the QEs relative position. (a) Normalized LDOS dependence on the separation, $|\mathbf{d}|$, between the emitters. Blue to yellow lines show $P_{II}^f(\omega)$ for $\boldsymbol{\mu}_E$ displaced horizontally (see inset). (b) Normalized LDOS dependence on the orientation of the relative position $\mathbf{d}$ between the QEs for a fixed separation $|\mathbf{d}| = 0.5$ nm. Black dotted line plots the bare cavity spectrum. (c) Weighted difference $(P_{II}^f(\omega) - P_I^f(\omega))/P_I^f(\omega)$ as a function of both ω and ω_E for the case where the distorting QE is displaced $|\mathbf{d}| = 0.5$ nm horizontally. (Darkest blue point in insets (a) and (b)). Grey solid line sets $\omega = \omega_E$. (NPoM with $D = 35$ nm and $\delta = 1.5$ nm).

Figure 3(b) shows how the LDOS is modified depending on the orientation of the relative position vector $\mathbf{d}$ ($|\mathbf{d}| = 0.5$ nm) with $\hat{\mathbf{n}}_\mu = \hat{\mathbf{n}}_E = \hat{\mathbf{n}}_z$. We consider five different orientations, with angular steps of $\pi/8$. As in figure 3(a), the colour code relates each spectrum with the distorting QE position in the inset. The apparent differences in the Purcell spectra originate from the spatial dependence of $\mathbf{G}_I(\mathbf{r}_E, \mathbf{r}, \omega)$ across the gap. While the vertical component of the plasmonic field at ω_1 is mainly uniform within the gap, the free-space contribution changes its sign around its centre. This gives rise to LDOS maxima at the low and high frequency sides of the bare cavity resonance, for horizontal and vertical QE–QE relative positions, respectively. In between these two configurations, around the position of the distorting QE that vanishes the free-space contribution to $\mathbf{G}_I(\mathbf{r}_E, \mathbf{r}, \omega)$, a symmetric dip emerges in the spectrum. Figure 3(c) analyzes the dependence of the Purcell factor on both ω and ω_E in terms of the weighted difference $(P_{II}^f(\omega) - P_I^f(\omega))/P_I^f(\omega)$ for the horizontal configuration with $|\mathbf{d}| = 0.5$ nm (see dark markers in panels (a) and (b)). This magnitude quantifies the effect of the distorting QE beyond the dipolar plasmon and within a broader frequency window. This map shows clearly that the distorting QE affects significantly the Purcell factor even when it is not at resonance with any plasmonic mode of the cavity. Differences between distorted and bare cavity LDOS are apparent at all frequencies, mainly, but not only, when the natural frequencies of both QEs overlap ($\omega = \omega_E$, grey line). Furthermore, as already commented above, the distorting QE can induce an increase or decrease in the Purcell factor depending on the system configuration.

4. Spectral density and mode decomposition

In order to elucidate the nature of the changes induced by the distorting QE into the cavity LDOS, we focus next into disentangling the different modal contributions to the spectral density, $J_{II}(\omega)$. This magnitude encodes the interaction strength between the probing QE and its EM environment. It can be written in terms of the Purcell factor $P_i^f(\omega)$ as $J_I(\omega) = \frac{\gamma_0}{2\pi} P_I^f(\omega)$, where $\gamma_0 = \omega^3 \mu^2/(3\pi\epsilon_0 \hbar c^3)$ is the decay rate of the probing QE in free-space. The Drude-like form of the metal permittivity and the high-quality resonator approximation allow us to express the Dyadic Green's function for the bare cavity as

$$\mathbf{G}_I(\mathbf{r}, \mathbf{r}', \omega) = \mathbf{G}_0(\mathbf{r}, \mathbf{r}', \omega) + \sum_n \mathbf{G}_n(\mathbf{r}, \mathbf{r}') \mathcal{L}_n(\omega), \tag{2}$$

where the first term is the free-space Dyadic Green's function. The second (scattering) one is decomposed into complex Lorentzian functions, $\mathcal{L}_n(\omega) = \frac{1}{(\omega_n - i\gamma_m/2) - \omega}$, centred at ω_n, the resonant frequency of plasmon

mode n, and whose width is given by the metal damping frequency, γ_{m} [23]. $\mathbf{G}_n(\mathbf{r},\mathbf{r}')$is the light–matter coupling tensor that weights the contribution of mode n and contains all the spatial information on the modal fields. Crucially, this term is mainly real. Thus, in bare nanocavities, where the second term in equation (2) dominates, the spectral density acquires the form of a sum of perfectly symmetric Lorentzian profiles, $J_{\mathrm{I}}(\omega)=\sum_n \frac{g_n^2}{\pi}\frac{\gamma_{\mathrm{m}}/2}{(\omega-\omega_n)^2+\gamma_{\mathrm{m}}^2/4}$ with $g_n^2 \propto \hat{\mathbf{n}}_\mu \mathbf{G}_n(\mathbf{r},\mathbf{r},\omega)\hat{\mathbf{n}}_\mu$ [23].

By introducing equation (2) into equation (1), we can obtain the spectral density experienced by the probing QE in the distorted cavity as $J_{\mathrm{II}}(\omega)=\frac{\gamma_0}{2\pi}P_{\mathrm{II}}^{\mathrm{f}}=J_{\mathrm{I}}(\omega)+J_{\mathrm{I-II}}(\omega)$, where the second term accounts for the effect of the second QE in the bare cavity LDOS. In general, (see appendix A for details) we can write

$$J_{\mathrm{I-II}}(\omega)=\frac{1}{\pi}\,\mathrm{Im}\left\{\sum_n \chi_{1,n}\mathcal{L}_n(\omega)+\sum_n \chi_{2,n}(\mathcal{L}_n(\omega))^2+\chi_{\mathrm{E}}\mathcal{L}_{\mathrm{E}}(\omega)\right\}. \tag{3}$$

Equation (3) shows clearly that $J_{\mathrm{II}}(\omega)$ does not have the same spectral form as $J_{\mathrm{I}}(\omega)$. The presence of $\boldsymbol{\mu}_{\mathrm{E}}$ in the bare cavity modifies the spectral density through three different physical mechanisms. Firstly, it alters the original plasmonic coupling strength constants, g_n^2, which are no longer real. Second, it induces modal-like plasmon interactions, yielding quadratic, $(\mathcal{L}_n(\omega))^2$, terms in the LDOS. Finally, the polarizability lineshape of the distorting QE, $\mathcal{L}_{\mathrm{E}}(\omega)$, also emerges naturally in the spectral density, as it does in the free-space configuration in figure 1(b). In the following section, we investigate how these different effects contribute to the results presented in figures 2 and 3 for a NPoM geometry.

4.1. NPoM cavity

Figures 4(a) and (b) show the different contributions to $J_{\mathrm{II}}(\omega)$ at the gap centre of a NPoM cavity with $D=35$ nm and $\delta=1.5$ nm (red lines). The distorting QE is displaced 0.5 nm horizontally (a) and vertically (b) from the probing one. The dipole moment of both emitters is oriented vertically. The spectral parameters are the same as in figure 3. The black line plots the spectrum for the bare cavity, $J_{\mathrm{I}}(\omega)$. The components of $J_{\mathrm{I-II}}(\omega)$ (cyan line) in equation (3) are plotted in dotted lines. The quadratic plasmonic Lorentzian contribution presents the same symmetric Lorentzian-like profile in both panels (orange). On the contrary, the terms altering the coupling strength of the bare cavity (blue) and the QE polarizability (green) are clearly asymmetric. This allows us to anticipate complex $\chi_{1,n}$ and χ_{E} amplitudes, as the asymmetries originate from the real part of the complex Lorentzian functions in equation (3). Note as well that these two mechanisms oppose each other in both panels, and present maxima (minima) that are slightly redshifted (blueshifted) with respect to $\omega=\omega_1$. This gives rise to the qualitative differences in the asymmetry of $J_{\mathrm{II}}(\omega)$ in both panels.

To explore the spatial dependence of the three contributions in $J_{\mathrm{I-II}}(\omega)$, we plot in figures 4(c) and (d) the real (solid lines) and imaginary (dashed lines) parts of their weights. $\chi_{1,1}$ and χ_{E} are normalized to g_1^2, the coupling strength for the bare cavity, while $\chi_{2,1}$ (note its different dimensionality), is normalized to $\gamma_{\mathrm{m}}g_1^2$. Similarly to figure 2(b), these amplitudes are evaluated at a fixed distance, $|\mathbf{d}|=0.5$ nm, and different QE–QE relative position orientations in figure 3(c), from vertical ($\theta=0$) to horizontal ($\theta=\pi/2$) alignments. We can observe that the real parts are rather insensitive to the orientation of $\mathbf{d}$ within the gap. As anticipated, $\chi_{2,1}$ is isotropic and purely imaginary, as a consequence of the uniform character of the resonant near-fields for the underlying capacitor-like plasmonic mode. Moreover, it is smaller than g_1^2 even at distances significantly shorter than the gap size ($|\mathbf{d}|=\delta/3$). On the contrary, uniform resonant plasmonic fields, inhomogeneous off-resonant modes and dipole-like free-space field components contribute to $\mathrm{Im}\{\chi_{1,1}\}$ and $\mathrm{Im}\{\chi_{\mathrm{E}}\}$. These are much larger and flip sign with θ, which gives rise to the qualitative differences in $J_{\mathrm{II}}(\omega)$ shown in figures 3(a) and (b). Both $\chi_{1,1}$ and χ_{E} involve products between the plasmonic fields and free-space components (see appendix A). The latter are the origin of the change of sign in the imaginary part of the amplitudes whereas the former provide an almost constant background, slightly stronger for $\theta\approx 0$ due to the interplay of bright and dark modes in the cavity. Finally, figure 4(d) renders the three amplitudes as a function of the QE–QE distance for $\theta=\pi/2$. Both real and imaginary parts decay with increasing $|\mathbf{d}|$, although the latter does so much faster. As a result, at 2–3 nm distances the three terms in equation (3) acquire a purely symmetric Lorentzian spectral shape. The negative sign of $\mathrm{Im}\{\chi_{\mathrm{E}}\}$ (the largest contribution) translates into a symmetric dip superimposed on $J_{\mathrm{I}}(\omega)$, accounting for the optical absorption by the distorting QE.

4.2. Bow-tie-like antenna

To show the general character and validity of our analysis, we apply the Green's function scattering formalism to a full three dimensional system. The cavity of choice is sketched in figure 5(a). It is composed by two free-standing metallic (same Drude permittivity as before) rounded cones with 15 nm diameter and 15 nm height. One of the cones is oriented vertically (z-axis), the other horizontally (y-axis), in a

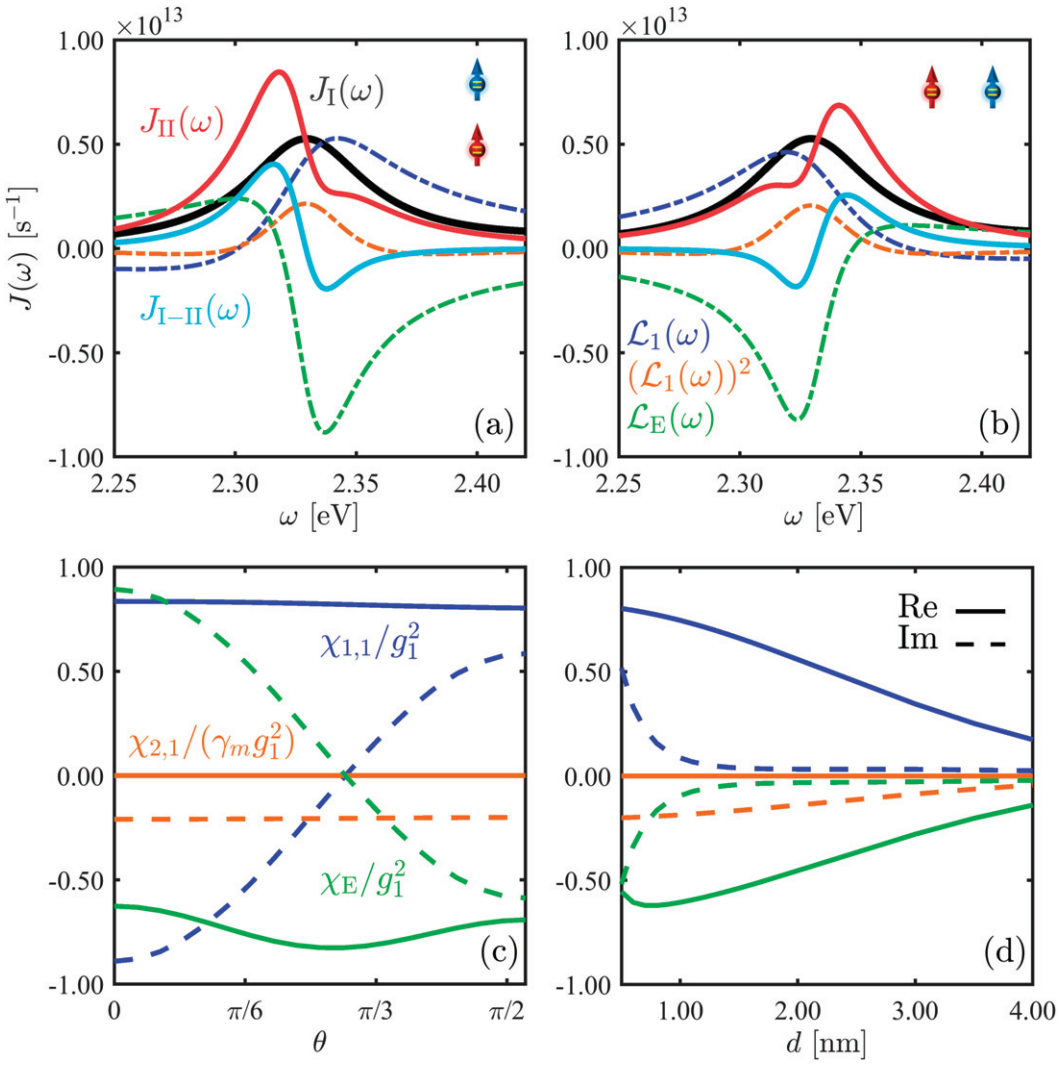

Figure 4. Modal decomposition of $J(\omega)$ at the gap centre of a distorted NPoM cavity ($D = 35$ nm, $\delta = 1.5$ nm) around $\omega = \omega_1$. (a) and (b) Bare and distorted spectral densities (solid lines) for vertical and horizontal QE–QE displacement ($|\mathbf{d}| = 0.5$ nm), respectively (both QEs are oriented vertically). Dotted lines plot the different contributions in $J_{\mathrm{I-II}}(\omega)$. (c) Modal weights of the different contributions in equation (3) versus the orientation of the QE–QE relative position ($\theta = 0$ corresponds to the vertical configuration). (d) Same as panel (c) but versus distance $|\mathbf{d}|$ for the horizontal case ($\theta = \pi/2$). In panels (c) and (d), solid (dashed) lines correspond to the real (imaginary) the part of the modal amplitudes, normalized to g_1^2 for the bare cavity.

bow-tie-like arrangement. Again, the dipole momenta of both QEs are oriented vertically. The probing emitter is placed 1 nm away from the vertices of both cones. The distorting one is displaced $|\mathbf{d}| = 2$ nm away along the positive z-direction. The Dyadic Green's functions of the bare structure, the only input required for the calculation of $J_{\mathrm{II}}(\omega)$ in our approach, are computed by means of numerical simulations performed using the finite-element solver of Maxwell's equations in COMSOL Multiphysics.

Figure 5(b) shows the Green's tensor components involved in the second term of equation (1), the real and imaginary parts of $\hat{\mathbf{n}}_z\mathbf{G}_{\mathrm{I}}(\mathbf{r}, \mathbf{r}_{\mathrm{E}}, \omega)\hat{\mathbf{n}}_z$ are plotted in dashed and solid blue lines, respectively. The green solid line renders $\mathrm{Im}\{\hat{\mathbf{n}}_z\mathbf{G}_{\mathrm{I}}(\mathbf{r}_{\mathrm{E}}, \mathbf{r}_{\mathrm{E}}, \omega)\hat{\mathbf{n}}_z\}$, which yields the depolarization correction to the free-space polarizability of the distorting QE. By direct inspection, several symmetric Lorentzian contributions can be identified in the imaginary spectra of figure 5(b), whereas a free-space background is apparent in $\mathrm{Re}\{\hat{\mathbf{n}}_z\mathbf{G}_{\mathrm{I}}(\mathbf{r}, \mathbf{r}_{\mathrm{E}}, \omega)\hat{\mathbf{n}}_z\}$. Both Green's functions were fitted using the form of equation (2), with the need of only five plasmonic modes. This fitting allows us to obtain $J_{\mathrm{I-II}}(\omega_0)$ and identify the contribution of the three terms in equation (3). Figure 5(c) shows the comparison between $\mathrm{Im}\{\tilde{\alpha}_{\mathrm{E}}(\omega)\}$ (dark) and $\mathrm{Im}\{\alpha_{\mathrm{E}}(\omega)\}$ (bright) for $\omega_{\mathrm{E}} = 2.20$ (red) and 2.45 eV (blue).

Figures 5(d) and (e) show spectral densities for two distorting QE frequencies, $\omega_{\mathrm{E}} = 2.20$ and 2.45 eV, respectively. In each panel, the bare cavity spectrum, $J_{\mathrm{I}}(\omega)$, is presented in black solid lines. It is calculated from $\mathrm{Im}\{\hat{\mathbf{n}}_z\mathbf{G}_{\mathrm{I}}(\mathbf{r}, \mathbf{r}, \omega)\hat{\mathbf{n}}_z\}$, obtained from full electrodynamic solutions for Maxwell's equations. The different contributions to $J_{\mathrm{I-II}}(\omega)$ are plotted by coloured dotted lines, and $J_{\mathrm{II}}(\omega)$ is shown in red solid line. For comparison, $J_{\mathrm{II}}(\omega)$ computed by means of COMSOL Multiphysics in which simulations modelling the

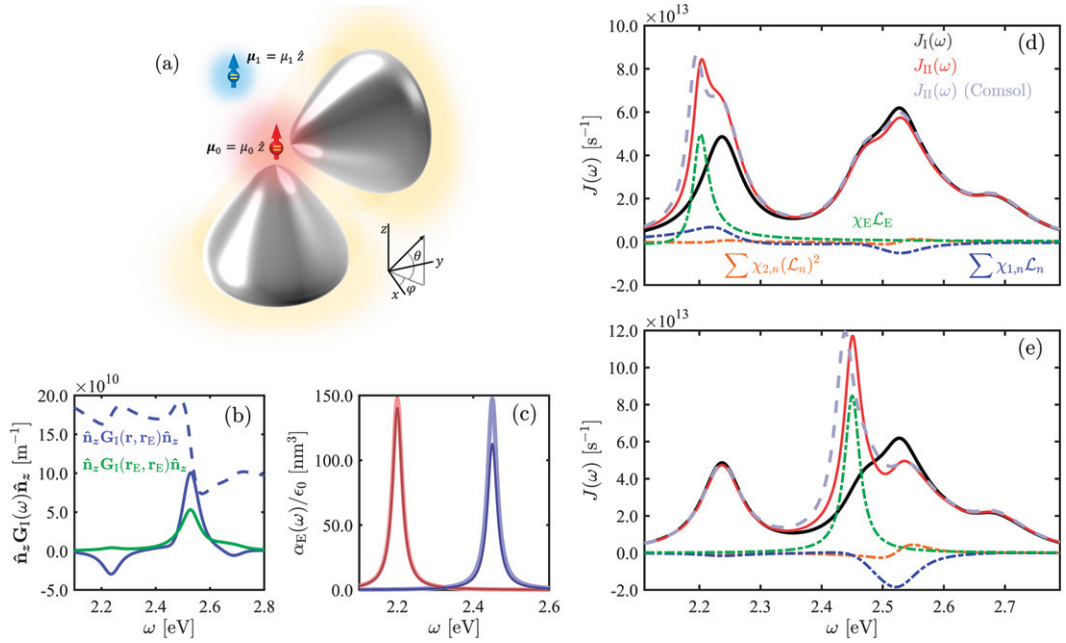

Figure 5. $J(\omega)$ distortion in a bow-tie cavity. (a) Sketch of the cavity formed by two rounded cones (15 nm height and diameter) and the position of the probing (red) and distorting (blue) QEs (both are oriented along z-direction). (b) Dyadic Green's function components involved in the calculation of $J_{\rm I-II}(\omega)$ in equation (3). (c) Imaginary part of $\alpha_{\rm E}(\omega)$ (bright) and $\tilde{\alpha}_{\rm E}(\omega)$ (dark) of QEs with $\omega_{\rm E} = 2.20$ (red) and 2.45 eV (blue). (d) Spectral density decomposition for $\omega_{\rm E} = 2.20$ eV. Solid lines correspond to $J_{\rm I}(\omega)$ (black) and $J_{\rm II}(\omega)$ (red), and dotted lines show the three contributions to $J_{\rm I-II}(\omega)$. Dashed light grey line sets the spectra obtained from numerical simulations using an effective permittivity modelling of the distorting QE. (e) Same as panel (d) but for $\omega_{\rm E} = 2.45$ eV.

distorting QE as dielectric sphere of permittivity $\epsilon_{\rm eff}(\omega)$ (see section 2.2) are rendered in light grey dashed line. We can observe that they are in very good agreement with the prediction from our approach. In both panels, the absorption lineshape of the distorting QE is clearly imprinted in the cavity LDOS. Therefore, and as expected for $|\mathbf{d}| = 2$ nm in figure 3(d), $\mathcal{L}_{\rm E}(\omega)$, with (mainly) real $\chi_{\rm E}$, dominates $J_{\rm I-II}(\omega_{\rm E})$. However, $\mathcal{L}_n(\omega)$ (blue) and $(\mathcal{L}_n(\omega))^2$ (orange) are not negligible either. Both yield asymmetric profiles with maxima and minima not (only) at the QE natural frequency, but in the vicinity the resonant plasmonic frequencies, $\omega_1 = 2.25$ eV and $\omega_4 = 2.56$ eV. Remarkably, panel (d) reveals that the coupling of the probing QE to this mode is significantly reduced by the distorting QE despite their considerable detuning, $\omega_4 - \omega_{\rm E} \gg \gamma_{\rm m}, \gamma_{\rm E}$.

4.3. Hamiltonian picture

In order to gain insight into equation (3) and the physical interpretation of the three terms contributing to $J_{\rm I-II}(\omega)$, we revisit here the hybrid QE-cavity system under a quantum description. This could be done taking into account the full richness of the plasmonic spectrum of the bare cavity, but, for simplicity, we will focus here on its single-mode version. The Hamiltonian for this simplified system reads

$$\begin{aligned}\hat{H} &= \hat{H}_\sigma + \hat{H}_{\rm cav} + \hat{H}_{\rm int} \\ &= \left(\omega\hat{\sigma}^\dagger\hat{\sigma}\right) + \left(\omega_n\hat{a}_n^\dagger\hat{a}_n + \omega_{\rm E}\hat{b}^\dagger\hat{b} + g_{n,{\rm E}}\hat{a}_n^\dagger\hat{b} + {\rm h.c.}\right) + \left(g_n\hat{a}_n^\dagger\hat{\sigma} + {\rm h.c.}\right), \end{aligned} \tag{4}$$

where the first, second and third terms correspond to the probing QE (modelled as a two-level system), its photonic environment (which involves the plasmon resonance, labelled as n, and the distorting QE) and their interaction, respectively. Thus, $\hat{a}_n$, $\hat{\sigma}$, and $\hat{b}$ are the annihilation operators for the cavity mode and the two QEs. Note that the distorting emitter has been bosonized, in agreement with our scattering theory description, in which it is treated as part of the LDOS. The plasmon mode is coupled to both QEs, with strengths g_n and $g_{n,{\rm E}}$, but the emitters are not interacting with each other.

Recently, a general approach has been proposed that sets the link between the Hamiltonian describing the interaction between a single QE and its photonic environment and the spectral density for the system, $J(\omega)$ [26, 58]. This framework, based on Fano diagonalization theory [59], is valid for Hamiltonians involving interacting modes, like equation (4). Applying this formalism to our system, we can obtain the spectral density for our system from the resolvent of the non-Hermitian Hamiltonian for the photonic environment, $\hat{H'}_{\rm env} = \hat{H}_{\rm env} - i\frac{\gamma_{\rm m}}{2}\hat{a}_n^\dagger\hat{a}_n - i\frac{\gamma_{\rm E}}{2}\hat{b}^\dagger\hat{b}$ (see appendix B).

In the regime of weak interaction between cavity and distorting QE ($g_{n,\mathrm{E}} \ll \omega_n, \omega_\mathrm{E}$), in which equation (1) is valid, we obtain an spectral density in which the effect of the distorting QE acquires exactly the same for as $J_{\mathrm{I-II}}(\omega)$ in equation (3). Thus, we can now express the modal amplitudes in this expression in terms of the parameters of the Hamiltonian in equation (5) as

$$\chi_\mathrm{E} = -\chi_{1,n} = \frac{g_n^2 g_{n,\mathrm{E}}^2}{(\tilde{\omega}_\mathrm{E} - \tilde{\omega}_n)^2}, \quad \chi_{2,n} = \frac{g_n^2 g_{n,\mathrm{E}}^2}{\tilde{\omega}_\mathrm{E} - \tilde{\omega}_n}, \tag{5}$$

where $\tilde{\omega}_n = \omega_n - i\gamma_\mathrm{m}/2$ and $\tilde{\omega}_\mathrm{E} = \omega_\mathrm{E} - i\gamma_\mathrm{E}/2$ are the complex cavity and QE frequencies that emerge naturally in $\hat{H}'_{\mathrm{env}}$.

Equation (5) shed light into the results presented above for distorted NPoM and bow-tie cavities. Firstly, they show that all modal amplitudes are proportional to $g_n^2 g_{n,\mathrm{E}}^2$, the square of the product of the plasmon–QE coupling constants. More importantly, they are complex, in general. As we already discussed, this yields a non-vanishing contribution of the real part of the complex Lorentzian functions in equation (3) to the LDOS of distorted cavities. Particularly, when plasmon resonance and QE natural frequency are at resonance, $\omega_n = \omega_\mathrm{E}$, $\mathrm{Re}\{\chi_{2,1}\} = 0$, which explains the imaginary character of this amplitude in figures 3(c) and (d) for all relative QE–QE positions. Furthermore, as predicted by equation (5), both the real and imaginary parts of $\chi_{1,1}$ and χ_E are, despite minor deviations, opposite in sign in these two panels. Finally, these single-mode amplitudes also help us interpret the findings in figure 5. Note that the plasmonic mode components to the various $J_{\mathrm{I-II}}(\omega)$ contributions cannot be disentangled in this case. However, focussing only on the distorting QE spectra, we can observe that it presents a slight asymmetry in panel (d), where the QE is close to resonance with the cavity mode at 2.22 eV, but it is fully symmetric in panel (e), where the QE is further from resonance with the mode at 2.52 eV. We can link this observation to the effect of cavity-QE detuning on χ_E in equation (5). Note that this is complex, with similar real and imaginary parts if $|\omega_n - \omega_\mathrm{E}| \sim \gamma_\mathrm{m}/2$, and becomes effectively real for $|\omega_n - \omega_\mathrm{E}| \gg \gamma_\mathrm{m}/2$. Thus, we can conclude that the off-resonant character of the distorting QE in figure 5(e) is behind its fully symmetric contribution to the LDOS.

5. Conclusions

To conclude, we have presented an insightful approach based on first-order EM scattering theory to investigate the distortion induced by a QE in the LDOS of a nanocavity. The presence of the distorting emitter, modelled through an effective polarizability, can modify strongly the spectrum of the bare nanostructure. We have shown that it can both enhance or suppress significantly the LDOS, even when it is not on resonance with any EM mode of the bare system. We have focussed our attention on two plasmonic geometries, a NPoM cavity and a bow-tie architecture. The quasistatic character of both structures enables us to perform a complex Lorentzian decomposition of their Dyadic Green's functions. This has allowed us to identify and isolate three different terms (and mechanisms) in their spectral densities that encode the emitter distortion: the modification of the bare plasmonic couplings, plasmon–plasmon interactions and the absorption of the emitter itself. Our scattering theory is tested against full numerical simulations accounting for the distorting emitter through an effective permittivity. Finally, we have developed a single-mode Hamiltonian interpretation of our findings, which sheds insights into our results in terms of well-defined parameters such as the plasmon–emitter coupling strengths and detunings. Our study reveal that the plasmon-mediated coupling between QEs in a nanocavity effectively gives rise to non-Lorentzian features in the density of states within the sub-wavelength regime that characterizes our system. We believe that our work offers a new perspective on QE interactions at the nanoscale. We emphasize the relevance of this work especially in the context of exciton transfer phenomena, quantum optical metamaterials, as well as on picocavity design and engineering, where sub-nanometer features alter greatly the LDOS.

Acknowledgments

This work was funded by the Spanish MINECO under Contract No. MDM-2014-0377-16-4 and from the Spanish Ministry for Science and Innovation under Contract No. RTI2018-099737-B-I00 and through the 'María de Maeztu' programme for Units of Excellence in R & D (CEX2018-000805-M). It was also supported by a Leonardo Grant for Researchers and Cultural Creators, BBVA Foundation. AM acknowledges support from the U.S. National Science Foundation (Grant DMR-1941680) and the Spanish MICINN (Grant TEM-FLU PID2019-109502GA-I00).

Data availability statement

All data that support the findings of this study are included within the article (and any supplementary files).

Appendix A. Expressions for the χ Lorentzian coefficients

In this appendix, we provide the expressions for the different χ amplitudes that arise in the Lorentzian decomposition of the LDOS. They can be written as:

$$\chi_i = \frac{\gamma_0 \Psi_0}{2\,\mathrm{Im}\{\widehat{\mathbf{n}}_\mu \mathbf{G}_0(\mathbf{r},\mathbf{r},\omega_i)\widehat{\mathbf{n}}_\mu\}} \widehat{\mathbf{n}}_\mu \mathbf{Q}_i \widehat{\mathbf{n}}_\mu, \tag{A.1}$$

where $\mathbf{Q}_i$ contains the different dependences, referring to the linear term ($i = 1, n$), the quadratic term ($i = 2, n$) and the distorting emitter contribution ($i = \mathrm{E}$). For each case, $\mathbf{Q}_i$ reads:

$$\mathbf{Q}_{1,n} = \frac{\mu_\mathrm{E}^2/\hbar}{1+\beta_\mathrm{I}(\mathbf{r}_\mathrm{E},\mathbf{r}_\mathrm{E},\omega_\mathrm{E})\mathrm{Im}\{\alpha_\mathrm{E}(\omega_\mathrm{E})\}} \frac{1}{\tilde{\omega}_\mathrm{E}-\tilde{\omega}_n} \left(\mathbf{G}_n(\mathbf{r},\mathbf{r}_\mathrm{E})\mathbf{T}(\hat{\mathbf{n}}_\mathrm{E})\mathbf{G}_0^\mathrm{T}(\mathbf{r},\mathbf{r}_\mathrm{E}) + \mathbf{G}_0(\mathbf{r},\mathbf{r}_\mathrm{E})\mathbf{T}(\hat{\mathbf{n}}_\mathrm{E})\mathbf{G}_n^\mathrm{T}(\mathbf{r},\mathbf{r}_\mathrm{E}) \right.$$
$$\left. + \sum_{m\neq n} \frac{\mathbf{G}_n(\mathbf{r},\mathbf{r}_\mathrm{E})\mathbf{T}(\hat{\mathbf{n}}_\mathrm{E})\mathbf{G}_m^\mathrm{T}(\mathbf{r},\mathbf{r}_\mathrm{E}) + \mathbf{G}_m(\mathbf{r},\mathbf{r}_\mathrm{E})\mathbf{T}(\hat{\mathbf{n}}_\mathrm{E})\mathbf{G}_n^\mathrm{T}(\mathbf{r},\mathbf{r}_\mathrm{E})}{\omega_m-\omega_n} - \frac{\mathbf{G}_n(\mathbf{r},\mathbf{r}_\mathrm{E})\mathbf{T}(\hat{\mathbf{n}}_\mathrm{E})\mathbf{G}_n^\mathrm{T}(\mathbf{r},\mathbf{r}_\mathrm{E})}{\tilde{\omega}_\mathrm{E}-\tilde{\omega}_n} \right), \tag{A.2}$$

$$\mathbf{Q}_{2,n} = \frac{\mu_\mathrm{E}^2/\hbar}{1+\beta_\mathrm{I}(\mathbf{r}_\mathrm{E},\mathbf{r}_\mathrm{E},\omega_\mathrm{E})\mathrm{Im}\{\alpha_\mathrm{E}(\omega_\mathrm{E})\}} \frac{\mathbf{G}_n(\mathbf{r},\mathbf{r}_\mathrm{E})\mathbf{T}(\hat{\mathbf{n}}_\mathrm{E})\mathbf{G}_n^\mathrm{T}(\mathbf{r},\mathbf{r}_\mathrm{E})}{\tilde{\omega}_\mathrm{E}-\tilde{\omega}_n}, \tag{A.3}$$

$$\mathbf{Q}_\mathrm{E} = \frac{(\mu_\mathrm{E}^2/\hbar)\left(\mathbf{G}_0(\mathbf{r},\mathbf{r}_\mathrm{E})\mathbf{T}(\hat{\mathbf{n}}_\mathrm{E})\mathbf{G}_0^\mathrm{T}(\mathbf{r},\mathbf{r}_\mathrm{E}) - \sum_n \mathbf{Q}_{1,n}\right)}{1+\beta_\mathrm{I}(\mathbf{r}_\mathrm{E},\mathbf{r}_\mathrm{E},\omega_\mathrm{E})\mathrm{Im}\{\alpha_\mathrm{E}(\omega_\mathrm{E})\}}, \tag{A.4}$$

where we have used $\tilde{\omega}_\mathrm{E} = \omega_\mathrm{E} - i\gamma_\mathrm{E}/2$ and $\tilde{\omega}_n = \omega_n - i\gamma_\mathrm{m}/2$.

Appendix B. Exact expression for the single-mode spectral density

Here, we provide the derivation of the exact expression for $J(\omega)$ obtained from the single-mode Hamiltonian in equation (4). To do so, we first express the non-Hermitian environment Hamiltonian as

$$\hat{H}'_\mathrm{env} = \begin{pmatrix}\hat{a}^\dagger & \hat{b}^\dagger\end{pmatrix} \mathbf{H}' \begin{pmatrix}\hat{a}\\ \hat{b}\end{pmatrix}, \quad \text{with } \mathbf{H}' = \begin{pmatrix}\omega_n - i\gamma_\mathrm{m}/2 & g_{n,\mathrm{E}}\\ g_{n,\mathrm{E}} & \omega_\mathrm{E} - i\gamma_\mathrm{E}/2\end{pmatrix}. \tag{B.1}$$

In a similar way, we rewrite the interaction Hamiltonian as

$$\hat{H}_\mathrm{int} = \begin{pmatrix}\hat{a}^\dagger & \hat{b}^\dagger\end{pmatrix} \mathbf{g}\hat{\sigma} + \mathrm{h.c.}, \quad \text{with } \mathbf{g} = \begin{pmatrix}g_n\\ 0\end{pmatrix}. \tag{B.2}$$

Let us stress that the origin of the complex frequencies in the Hamiltonian above resides in the master equation description of the system. This includes Lindblad operators, $L_{n,E}[\hat{\rho}]$, accounting for the dissipation experienced by the cavity (with rate γ_m) and the distorting QE (with rate γ_E), $\partial_t\hat{\rho} = i[\rho,\hat{H}] + \frac{\gamma_\mathrm{m}}{2}L_n[\hat{\rho}]$ $+ \frac{\gamma_\mathrm{E}}{2}L_\mathrm{E}[\hat{\rho}]$. We can now express the spectral density in terms of the resolvent matrix as [26, 58]

$$J(\omega) = \frac{1}{\pi}\,\mathrm{Im}\left\{\mathbf{g}^\mathrm{T}\left(\mathbf{H}' - \mathbf{I}\omega\right)^{-1}\mathbf{g}\right\} = \frac{1}{\pi}\frac{g_n^2(\tilde{\omega}_\mathrm{E}-\omega)}{(\tilde{\omega}_n-\omega)(\tilde{\omega}_\mathrm{E}-\omega) - g_{n,\mathrm{E}}^2}. \tag{B.3}$$

By keeping only the first-order correction in the Taylor expansion at $g_{n,\mathrm{E}}^2 = 0$ of the spectral density above, we obtain $J(\omega) = J_\mathrm{I}(\omega) + J_{\mathrm{I-II}}(\omega)$ with

$$J_\mathrm{I}(\omega) = \frac{1}{\pi}g_n^2\mathcal{L}_n(\omega), \tag{B.4}$$

and

$$J_\mathrm{II}(\omega) = \frac{1}{\pi}\left(\frac{g_n^2 g_{n,\mathrm{E}}^2}{(\tilde{\omega}_\mathrm{E}-\tilde{\omega}_n)^2}\mathcal{L}_\mathrm{E}(\omega) - \frac{g_n^2 g_{n,\mathrm{E}}^2}{(\tilde{\omega}_\mathrm{E}-\tilde{\omega}_n)^2}\mathcal{L}_n(\omega) + \frac{g_n^2 g_{n,\mathrm{E}}^2}{\tilde{\omega}_\mathrm{E}-\tilde{\omega}_n}(\mathcal{L}_n(\omega))^2\right). \tag{B.5}$$

Note that this last spectral density is the single-mode version of equation (3), which allows us to extract the expressions for the modal amplitudes given in equation (5).

ORCID iDs

Alvaro Cuartero-González https://orcid.org/0000-0002-8272-5341
Alejandro Manjavacas https://orcid.org/0000-0002-2379-1242
Antonio I Fernández-Domínguez https://orcid.org/0000-0002-8082-395X

References

[1] Benz F *et al* 2016 *Science* **354** 726–9
[2] Laing S, Jamieson L E, Faulds K and Graham D 2017 *Nat. Rev. Chem.* **1** 1–19
[3] Bodelón G *et al* 2016 *Nat. Mater.* **15** 1203–11
[4] Nie S and Emory S R 1997 *Science* **275** 1102–6
[5] Kneipp K, Wang Y, Kneipp H, Perelman L T, Itzkan I, Dasari R R and Feld M S 1997 *Phys. Rev. Lett.* **78** 1667
[6] van Schrojenstein Lantman E M, Deckert-Gaudig T, Mank A J G, Deckert V and Weckhuysen B M 2012 *Nat. Nanotechnol.* **7** 583–6
[7] Trügler A and Hohenester U 2008 *Phys. Rev.* B **77** 115403
[8] Delga A, Feist J, Bravo-Abad J and Garcia-Vidal F 2014 *Phys. Rev. Lett.* **112** 253601
[9] Andersen M L, Stobbe S, Sørensen A S and Lodahl P 2011 *Nat. Phys.* **7** 215–8
[10] Neuman T, Esteban R, Casanova D, García-Vidal F J and Aizpurua J 2018 *Nano Lett.* **18** 2358–64
[11] Cuartero-González A and Fernández-Domínguez A I 2018 *ACS Photonics* **5** 3415–20
[12] Sanders S, May A, Alabastri A and Manjavacas A 2018 *ACS Photonics* **5** 3282–90
[13] Muniz Y, Manjavacas A, Farina C, Dalvit D and Kort-Kamp W 2020 *Phys. Rev. Lett.* **125** 033601
[14] Giannini V, Fernaíndez-Domínguez A I, Heck S C and Maier S A 2011 *Chem. Rev.* **111** 3888–912
[15] Sanders S and Manjavacas A 2018 *ACS Photonics* **5** 2437–45
[16] Haugland T S, Schäfer C, Ronca E, Rubio A and Koch H 2021 *J. Chem. Phys.* **154** 094113
[17] Hamza A O, Viscomi F N, Bouillard J-S G and Adawi A M 2021 *J. Phys. Chem. Lett.* **12** 1507–13
[18] Li R Q, Hernángomez-Pérez D, García-Vidal F and Fernández-Domínguez A I 2016 *Phys. Rev. Lett.* **117** 107401
[19] González-Tudela A, Huidobro P, Martín-Moreno L, Tejedor C and García-Vidal F 2014 *Phys. Rev.* B **89** 041402
[20] Hümmer T, García-Vidal F, Martín-Moreno L and Zueco D 2013 *Phys. Rev.* B **87** 115419
[21] Varguet H, Rousseaux B, Dzsotjan D, Jauslin H R, Guérin S and Colas des Francs G 2016 *Opt. Lett.* **41** 4480–3
[22] Hughes S, Richter M and Knorr A 2018 *Opt. Lett.* **43** 1834–7
[23] Cuartero-González A and Fernández-Domínguez A I 2020 *Phys. Rev.* B **101** 035403
[24] Sauvan C, Hugonin J P, Maksymov I and Lalanne P 2013 *Phys. Rev. Lett.* **110** 237401
[25] Pellegrino D *et al* 2020 *Phys. Rev. Lett.* **124** 123902
[26] Medina I, García-Vidal F J, Fernández-Domínguez A I and Feist J 2021 *Phys. Rev. Lett.* **126** 093601
[27] Franke S, Hughes S, Dezfouli M K, Kristensen P T, Busch K, Knorr A and Richter M 2019 *Phys. Rev. Lett.* **122** 213901
[28] Ren J, Franke S and Hughes S 2021 arXiv:2101.07633
[29] Sanders S and Manjavacas A 2020 *Nanophotonics* **9** 473–80
[30] Holzmeister P, Pibiri E, Schmied J J, Sen T, Acuna G P and Tinnefeld P 2014 *Nat. Commun.* **5** 1–9
[31] Kern J *et al* 2012 *Nano Lett.* **12** 5504–9
[32] Zhu W and Crozier K B 2014 *Nat. Commun.* **5** 1–8
[33] Zhu W, Esteban R, Borisov A G, Baumberg J J, Nordlander P, Lezec H J, Aizpurua J and Crozier K B 2016 *Nat. Commun.* **7** 1–14
[34] Antosiewicz T J, Apell S P and Shegai T 2014 *ACS Photonics* **1** 454–63
[35] Chikkaraddy R *et al* 2016 *Nature* **535** 127–30
[36] Leng H, Szychowski B, Daniel M C and Pelton M 2018 *Nat. Commun.* **9** 1–7
[37] Gurlek B, Sandoghdar V and Martín-Cano D 2018 *ACS Photonics* **5** 456–61
[38] Denning E V, Iles-Smith J and Mork J 2019 *Phys. Rev.* B **100** 214306
[39] Wallraff A, Schuster D I, Blais A, Frunzio L, Huang R S, Majer J, Kumar S, Girvin S M and Schoelkopf R J 2004 *Nature* **431** 162–7
[40] Hoang T B, Akselrod G M and Mikkelsen M H 2016 *Nano Lett.* **16** 270–5
[41] Bogdanov S *et al* 2017 *Phys. Rev.* B **96** 035146
[42] Sáez-Blázquez R, Feist J, Fernández-Domínguez A I and García-Vidal F J 2017 *Optica* **4** 1363–7
[43] Alaee R, Gurlek B, Albooyeh M, Martín-Cano D and Sandoghdar V 2020 *Phys. Rev. Lett.* **125** 063601
[44] Guimond P O, Grankin A, Vasilyev D, Vermersch B and Zoller P 2019 *Phys. Rev. Lett.* **122** 093601
[45] Aubry A, Lei D Y, Maier S A and Pendry J B 2011 *ACS Nano* **5** 3293–308
[46] Lei D Y, Aubry A, Maier S A and Pendry J B 2010 *New J. Phys.* **12** 093030
[47] Loudon R 2000 *The Quantum Theory of Light* (Oxford: Oxford University Press)
[48] Novotny L and Hecht B 2012 *Principles of Nano-Optics* (Cambridge: Cambridge University Press)
[49] Carminati R, Greffet J-J, Henkel C and Vigoureux J M 2006 *Opt. Commun.* **261** 368–75
[50] Marinchio H, Carminati R, García-Martín A and Sáenz J J 2014 *New J. Phys.* **16** 015007
[51] Albaladejo S, Gómez-Medina R, Froufe-Pérez L S, Marinchio H, Carminati R, Torrado J F, Armelles G, García-Martín A and Sáenz J J 2010 *Opt. Express* **18** 3556–67
[52] Aubry A, Lei D Y, Maier S A and Pendry J 2010 *Phys. Rev.* B **82** 205109
[53] Passarelli N, Bustos-Marún R and Depine R 2019 *J. Phys. Chem.* C **123** 13015–26
[54] Kewes G, Binkowski F, Burger S, Zschiedrich L and Benson O 2018 *ACS Photonics* **5** 4089–97
[55] Bohlen J, Cuartero-González Á, Pibiri E, Ruhlandt D, Fernández-Domínguez A I, Tinnefeld P and Acuna G P 2019 *Nanoscale* **11** 7674–81
[56] Gonzalez-Ballestero C, Feist J, Moreno E and Garcia-Vidal F J 2015 *Phys. Rev.* B **92** 121402
[57] Sáez-Blázquez R, Feist J, García-Vidal F J and Fernández-Domínguez A I 2020 *Adv. Opt. Mater.* **8** 2001447
[58] Dalton B, Barnett S M and Garraway B 2001 *Phys. Rev.* A **64** 053813
[59] Glutsch S 2002 *Phys. Rev.* B **66** 075310